Vacuum 168 (2019) 108860

Contents lists available at ScienceDirect

Vacuum

journal homepage: www.elsevier.com/locate/vacuum

Deposition rate effect on microstructure and perpendicular magnetic anisotropy of iron films prepared by ion-beam-assisted deposition

N.M. Lyadov[a,*], F.G. Vagizov[b], I.R. Vakhitov[b], A.I. Gumarov[b], Sh.Z. Ibragimov[b], D.M. Kuzina[b], I.A. Faizrakhmanov[a], R.I. Khaibullin[a], V.A. Shustov[a]

[a] Zavoisky Physical-Technical Institute, FRC Kazan Scientific Center of RAS, 420029, Kazan, Russia
[b] Kazan Federal University, 420008, Kazan, Russia

ARTICLE INFO

Keywords:
Ion-beam-assisted deposition
Iron films
Disordered and nanocrystalline structure
Magnetic anisotropy

ABSTRACT

Thin films of iron with different thickness (~40–300 nm) were deposited on quartz and silicon substrates by using ion beam assisted deposition (IBAD) technique. The influence of film thickness and deposition rate on microstructure, magnetic phase composition and perpendicular magnetic anisotropy (PMA) of iron films were studied by electron microscopy, X-ray diffraction, Mössbauer spectroscopy, vibrating-sample magnetometry and differential thermomagnetic analysis. Shown, that phase composition and magnetic properties of films depend substantially on the deposition rate, and, in fact, don't depend on both film thickness and the type of substrate. The strong PMA is observed in iron films formed at low (~3 nm/min) and medium (~10 nm/min) deposition rates only. The microstructure is characterized by the presence of nanocrystalline grains of α-Fe phase, as well as a significant fraction of disordered iron phase and nonmagnetic oxide phase of FeO (up to 20%). The FeO phase occurs due to the reaction of iron atoms with the residual atmosphere of the vacuum chamber. Moreover, significant positive deformation (about 3%) of crystal lattice of α-Fe grains was observed. The effect of deposition rate on the crystallinity, phase composition and PMA in thin iron films we associate with the features of the IBAD process.

1. Introduction

Ferromagnetic thin films with the perpendicular magnetic anisotropy (PMA) are of interest in magnetic storage devices industry and spintronics [1,2], as well in a relatively new field of research – straintronics [3]. From this point of view, such films are intensively studied in the last two decades (see, e.g., Refs. [4–11]). Magnetic films with PMA can be prepared by various methods and they differ in the elemental and phase compositions, microstructure and thickness, as well as the physical origin and the mechanisms of the appearance of PMA. Firstly, the ultra-thin epitaxial films with a thickness of several atomic layers should be emphasized [4,5]. Here, the PMA is usually associated with canted-spin configurations on the surface and/or film-substrate interface, as well with the lattice mismatch between the film and substrate that result in inhomogeneous mechanical stresses near the interface [6]. With increasing film thickness, the effect of the surface and interface decreases, so the in-plane anisotropy becomes preferable. As a result, the magnetization vector changes its direction with respect to the film plane from the «out-of-plane» to the «in-plane» orientation (the spin reorientation transition, SRT). However, the reverse SRT is also possible, in which the direction of the magnetization vector, on the contrary, changes from the “in-plane” to the “out-of-plane” orientation with increasing film thickness [7–11]. For amorphous and polycrystalline films of transition-metal element-based compounds, the appearance of PMA with increasing film thickness is associated with the growth of a clearly defined columnar grain microstructure in the film [7–9]. So the PMA origin is associated with the shape anisotropy of columns growing preferentially along the normal to the film plane. In the case of single- crystal nickel films, inverse SRT was explained by the increase in the strain-induced volume anisotropy [10]. In general, the stresses occurring in the films and/or the interface play an important role in the formation of the magnetic anisotropy. Note that the compression stresses or tensile strains in magnetic films can be produced additionally by introducing impurity atoms during the film deposition. For example, thin films of the FeCo alloy with the Al, O, and N impurity reveal the magnetic anisotropy perpendicular to the surface and a characteristic stripe domain structure after nitrogen atoms filling up interstitial space [11].

The composite cobalt oxide films CoO_x ($d \cong 0.8–2$ μm) with metallic cobalt nanoparticles exhibit pronounced PMA as well [9]. The work [9]

* Corresponding author.
E-mail address: nik061287@mail.ru (N.M. Lyadov).

https://doi.org/10.1016/j.vacuum.2019.108860
Received 29 January 2019; Received in revised form 2 August 2019; Accepted 6 August 2019
Available online 06 August 2019
0042-207X/

is of particular interest in the context of our results for the iron films. In Ref. [9], the composite CoO_x film was deposited by cobalt target sputtering using a gas mixture (Ar + O_2) with a controlled partial oxygen pressure. The dependences of the saturation magnetization M_s, coercive force H_c and PMA energy (K_A – anisotropy constant) of thin films on the gas pressure (Ar + O_2) and the partial oxygen pressure at the deposition were obtained. It was found that the composite CoOx film has a columnar structure. It was assumed that PMA appears due to the large contribution of the magnetocrystalline anisotropy of metallic Co with the hexagonal structure.

It is clear that the structural and magnetic properties of films essentially depend on the methods and conditions of their formation. Ion-beam-assisted deposition (IBAD) is one of well-known and widely used methods for the preparation of films on the different substrates. Earlier, we used this method to synthesize and modify diamond-like carbon films [12], to form silver nanoparticles in the silicate glass matrix [13], to produce nanocomposite multiferroic films based on barium titanate with magnetic cobalt nanoparticles [14], to obtain thin germanium layers [15,16] and nanostructured thin ZnO and Al_2O_3 films [17]. Moreover, recently we reported about the unusual properties of a thin iron film IBAD-deposited on the glass substrate [18]. The iron film had the thickness of 120 nm and the nanocrystalline structure with a noticeable fraction of iron atoms in a disordered state. The film had the large tensile microstrain of 2–3% exceeding the elastic deformation limit of iron and revealed the high perpendicular magnetic anisotropy unexpected for iron films with a thickness of 100 nm. The residual mechanical stresses in the film were removed after high-temperature annealing in vacuum, and the annealed sample exhibited the magnetic behavior typical for polycrystalline iron films with the in-plane anisotropy.

To shed more light on the origin of the perpendicular magnetic anisotropy observed in iron film [18], in this work we prepared an extensive series of thin-film Fe samples enriched by ^{57}Fe isotope using the IBAD technique. The iron films with different thicknesses were deposited on amorphous quartz and crystalline silicon substrates at different deposition rates. The iron films enriched by ^{57}Fe isotope were manufactured in order to use Mössbauer spectroscopy for the determination of Fe-based phases in the samples. Note that the isotopic composition of the iron films does not affect their structural and magnetic properties. It is known that magnetic properties of iron are due to the exchange interaction of the 3d electrons of the iron atoms, which is independent of the type of the isotope (^{56}Fe or ^{57}Fe). The effect of the deposition regime, film thickness and the type of substrate on the structural and magnetic properties of iron films was studied in detail to establish the correlations between the perpendicular magnetic anisotropy and structural features of as-deposited iron films.

1.1. Experimental

Thin iron films enriched by ^{57}Fe isotope were deposited on quartz glass and Si (111) substrates using the IBAD technique. In addition, control experiments on the deposition of iron films with a natural isotopic composition in order to show no effect of the isotopic composition of the films on their magnetic properties were carried out. Fig. 1 shows schematically the process of the deposition of thin films. The wide aperture Kaufman type ion source (diameter of 100 mm) with a diverging ion beam (divergence angle of ~10°) was used for the deposition of thin iron films. The ion source was used to sputter a 65 mm diameter foil of the metallic iron (pure: 99.998%) enriched by ^{57}Fe isotope and to perform ion-assisted deposition of films at the grazing angle of the ion incidence on the film surface ($\alpha_1 \cong 2°$). The nat-Fe target (pure: 99.98%) with a diameter of 65 mm was used for control experiments. Chemically pure xenon (99.995%) was used as the working gas. The energy of xenon ions varied in the range of 1–1.5 keV and the ion current density J was in the range of 65–200 μA/cm^2. The ion current density was measured in the region of the target using two Faraday

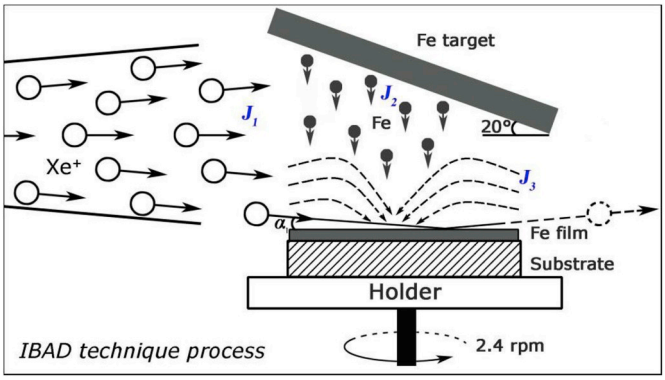

Fig. 1. Schematic illustration of thin film deposition using the IBAD technique, where J_1 is the flux of accelerated xenon ions, J_2 is the flux of sputtered iron atoms and J_3 is the flux of atoms of residual atmosphere (carbon, oxygen and xenon) in the vacuum chamber.

cylinders supplemented by two permanent magnets in order to avoid the secondary electron emission. The films were deposited in the vacuum of ~$2{\cdot}10^{-2}$ Pa. We emphasize that due to the importance of vacuum conditions, all iron films were deposited at the same vacuum: 10^{-3} Pa before and $2{\cdot}10^{-2}$ Pa after venting of the working gas into the ion source. The vacuum chamber was pumped out by two diffusion pumps with nitrogen traps. The composition and partial pressure of the residual gases in the vacuum chamber were not measured because of the lack of necessary equipment. The temperature of substrates did not exceed 50 °C during the deposition. The iron films were prepared in a wide range of the deposition rates of ~3–20 nm/min by changing ion current density and energy of xenon ions. The films prepared at three deposition rates were studied in detail: 3.2 (E = 1 keV, J = 65 μA/cm^2), 10 (E = 1,3 keV, J = 200 μA/cm^2) and 20 nm/min ((E = 1,5 keV, J = 200 μA/cm^2) The film thickness was varied in the range of ~40–300 nm.

To prepare iron films with the reproducible structural and magnetic properties, such deposition parameters as the distance from the target to the substrate, the angle of the ion beam incidence on the target and the distance from the target to the ion source were the same in all experiments.

Before deposition, the substrate and target were cleaned by ion irradiation at the angle of 20^0 for 3 min. Then the substrate gradually (with the increment of 3 min) was returned to the horizontal position. The ion beam irradiation was not interrupted. This treatment of the substrate guaranteed good adhesion of the films.

The elemental composition, thickness and surface morphology of iron films were studied on a scanning electron microscope (SEM, *Zeiss EVO 50 XVP*) equipped with an X-Ray energy dispersive spectrometer (EDX, *Inca energy-350*). Structural parameters and magnetic phase composition were studied by X-Ray diffraction (Cuk$_\alpha$ XRD, *DRON-7* with β – filter) in Bragg and grazing geometries and by conversion electron Mössbauer spectroscopy (CEMS, *WissEl spectrometer*). Conversion electrons were recorded using a gas-flow detector (*RiKon-5*). The velocity scale of the Mössbauer spectrometer was calibrated using a metallic iron spectrum taken at room temperature. Isomeric shifts were determined relative to the center of gravity of the α-Fe spectrum.

Magnetic properties were studied using vibrating-sample magnetometry (VSM) and differential thermomagnetic analysis (DTMA) [19,20]. Square samples of 5 × 5 mm^2 were used to minimize the effect of the sample shape on magnetic VSM measurements. The dependences of the induced magnetic moment on the magnetic field applied in the plane (in-plane geometry) or perpendicular to the plane (out-of-plane geometry) of the sample were recorded at room temperature with a magnetic field sweep of up to 500 mT. Diamagnetic contributions from quartz or silicon substrates were subtracted and the recorded magnetic

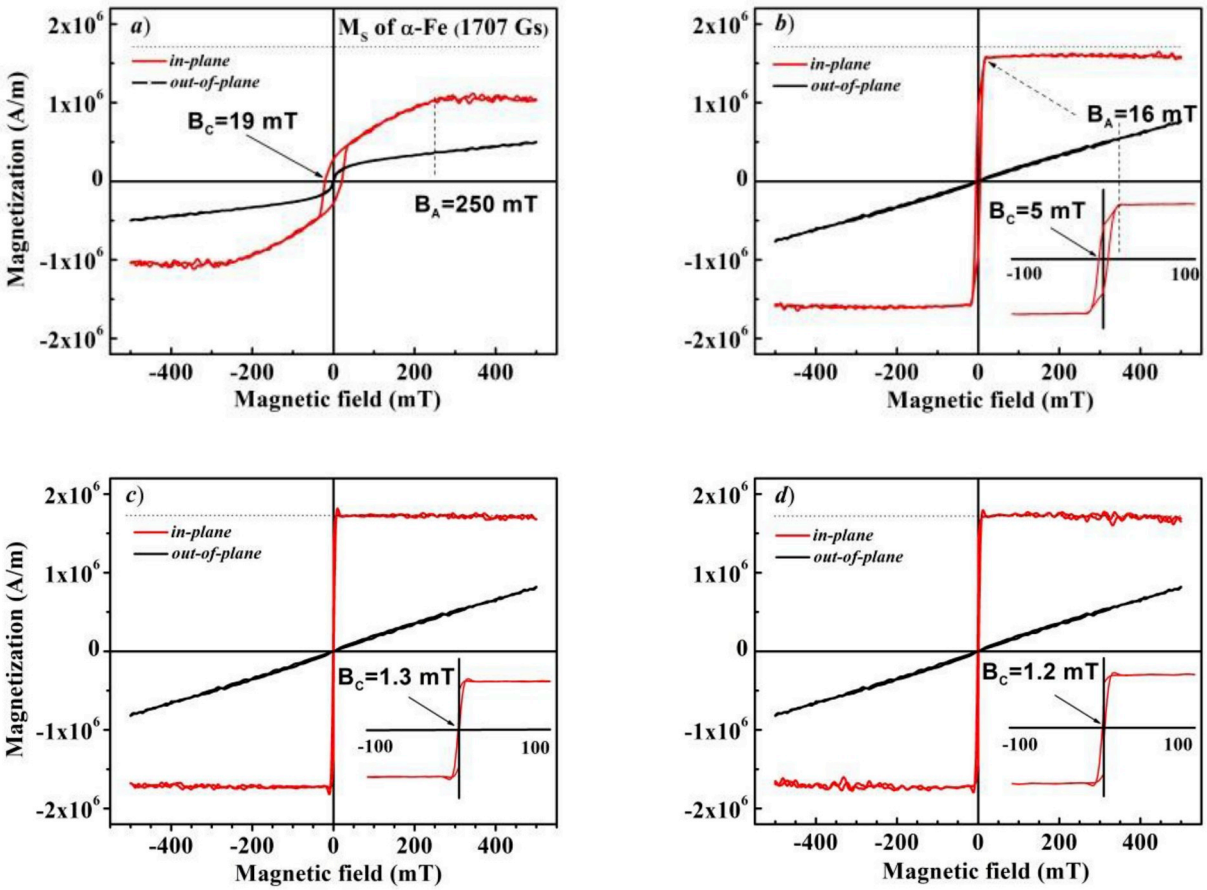

Fig. 2. Magnetic hysteresis loops for the in-plane and out-of-plane geometry of thin iron films prepared on quartz substrates at different deposition rates of a) 3.2 (d = 130 nm), b) 10 (d = 150 nm) and c) 20 nm/min (d = 160 nm), d) 20 nm/min, nat-Fe (d = 150 nm). Insets show the hysteresis loops at the low magnetic field sweep.

moment was normalized to the volume of the measured samples to calculate and compare the magnetization of iron films with different thicknesses. For DTMA studies, the samples were coated additionally with a 400 nm thick silicon layer in order to reduce their oxidation during the measurement by fast heating of samples with the rate of 100 K/min in the applied magnetic field of 300 mT.

2. Results and discussion

2.1. The observation of the perpendicular magnetic anisotropy

The basic feature of the prepared films is that they have the perpendicular magnetic anisotropy, the value of which depends strongly on the deposition rate. Fig. 2 shows the magnetic hysteresis loops recorded "in-plane" and "out-of-plane" of iron films deposited on quartz substrates at the deposition rates of 3.2, 10 and 20 nm/min. The iron film prepared at the low deposition rate of 3.2 nm/min shows a particular shape of the magnetic hysteresis loop called in the literature as the "transcritical hysteresis loop" [21]. It displays a moderate remanence with the high coercive force of $B_c \cong 19$ mT and a linear growth of the magnetization up to saturation with the increase in the applied magnetic field. The hysteresis loop shape with the linear growth of the magnetization before saturation is typical for magnetic films with the PMA [7,8,11,21]. The anisotropy field (B_A) at which the sample reaches its saturation (shown by dashed lines in Fig. 2) is directly connected to the PMA value (K_A) by the expression: $KA = M_S B_A/2$ [7], where M_S is the saturation magnetization. It is clearly seen in Fig. 2a that the iron film prepared at the low deposition rate reveals the strong PMA with the anisotropy field of $B_A \cong 250$ mT. However, the saturation magnetization of this film is approximately 20–30% less than that for the α-phase Fe (shown by the dotted line in Fig. 2). Note that the magnetization saturation is not reached even at the maximum magnetic field sweep of 500 mT during scanning of the field along the normal to the sample plane (out-of-plane geometry).

With the increase in the deposition rate, the remanence increases, and the saturation magnetization of films becomes comparable with the tabulated value for α-phase bulk Fe (see Fig. 2b and c). The anisotropy field and coercivity decrease rapidly to $B_A \cong 16$ mT and $B_c \cong 5$ mT in the iron film prepared at the medium deposition rate of 10 nm/min. The film prepared at the highest deposition rate used in our experiments exhibits the magnetic hysteresis loop typical for nanocrystalline (or amorphous) iron films with the high residual magnetization and very low coercive force $B_c \sim 1.0$–1.5 mT. In this case, the linear slope of the magnetization in the magnetic hysteresis loop disappears completely. This indicates that the PMA contribution to the magnetic energy of the film is zero, i.e., $B_A = 0$.

The magnetic hysteresis loop for the iron film with a thickness of 150 nm deposited at the same conditions (V = 20 nm/min) using the nat-Fe target is shown in Fig. 2. The deposition mode was chosen in such a way that the vacuum conditions in the working chamber minimally affected the elemental composition of iron films. It is seen that the hysteresis loops shown in Fig. 2c and d, differ little that proves the absence of the effect of the isotopic composition of the iron film on its characteristics studied in this work.

The results of VSM measurements of all samples made it possible to plot the experimental dependences of the anisotropy field and coercive force on the deposition rate in detail (Fig. 3). It can be seen that the anisotropy field and coercive force decrease fast with increasing

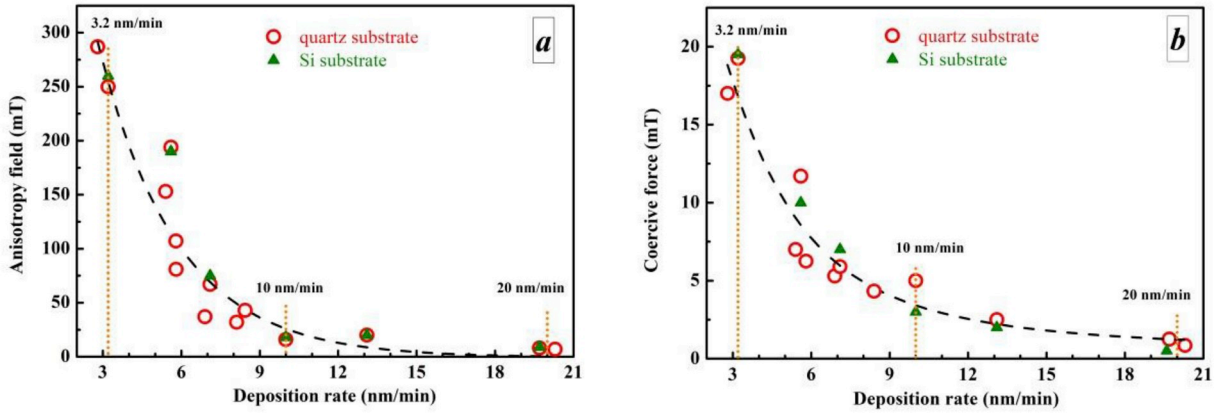

Fig. 3. Dependences of the anisotropy field (a) and the coercive force (b) on the deposition rate for iron films deposited on quartz (open circles) or silicon (filled triangles) substrates. Dotted (orange) lines show the deposition rate for which the element-phase compositions were studied in detail. (For interpretation of the references to colour in this figure legend, the reader is referred to the Web version of this article.)

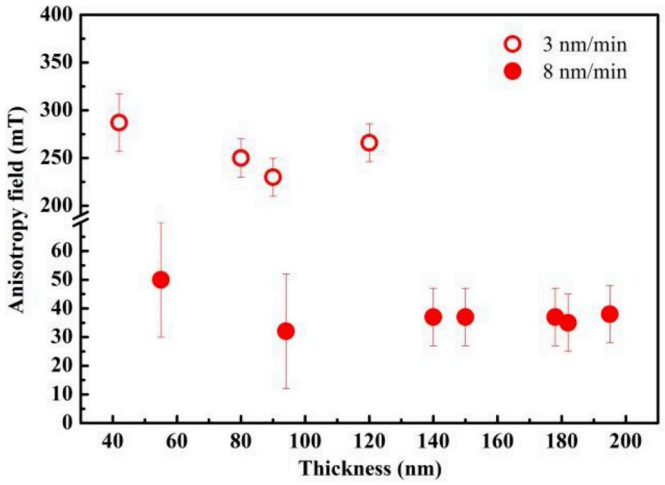

Fig. 4. Anisotropy field dependences on the thickness of iron films deposited on the quartz substrate at two deposition rates of 8.0 ± 0.5 and 3.0 ± 0.5 nm/min.

deposition rate, and they do not depend on the type of the substrate. Moreover, these quantities do not depend on the film thickness (Fig. 4).

An additional experiment was carried out in order to eliminate the effect of the substrate and interface-induced macrostress on PMA in the iron film. The Fe film with a thickness of about 60 nm was deposited on a single-crystal NaCl plate at the low deposition rate of 3.5 nm/min. Then this sample was placed in distilled water, where the NaCl substrate was completely dissolved, and the substrate-free Fe film was placed on a copper mesh. The VSM measurement showed that the free Fe film exhibits a transcritical hysteresis loop with the remanence, coercivity force and anisotropy field values, which are similar to those for the film as-deposited on the NaCl substrate. Thus, we may conclude that the PMA is induced by the intrinsic microstructure of the iron film. We studied in detail the elemental and phase compositions of three films exhibiting different magnetic behavior (Fig. 2) to establish the origin of perpendicular magnetic anisotropy in the iron film.

2.2. SEM studies and elemental composition

SEM in-plane and cross-section studies showed that the surface morphology of all films is smooth without any special microstructure features (e.g., columnar structures) in the cross-section image of the films at the SEM resolution of about 10 nm. However, the EDX elemental analysis of the samples showed that the oxygen content is 20, 10, and 3.5 at.% for the films prepared at the deposition rates of 3.2, 10, and 20 nm/min, respectively. The carbon content was in the range of 6–8 at.% for all three films. No other chemical elements except iron were detected. Thus, the high magnetic anisotropy in films obtained at the low deposition rate can be associated with the capture of oxygen atoms from residual atmosphere of the vacuum chamber during the deposition.

2.3. Magnetic phase composition

The analysis of CEMS spectra (Fig. 50 showed that the magnetic phase composition of iron films changes as a function of the deposition rate. Three sextets (ferromagnetic phases) marked by lines 1–3 in Fig. 5a and a paramagnetic doublet (line 4) can fit the CEMS spectrum of the iron film prepared at the low deposition rate of 3.2 nm/min. In the case of medium and high deposition rates of 10 nm/min and 20 nm/

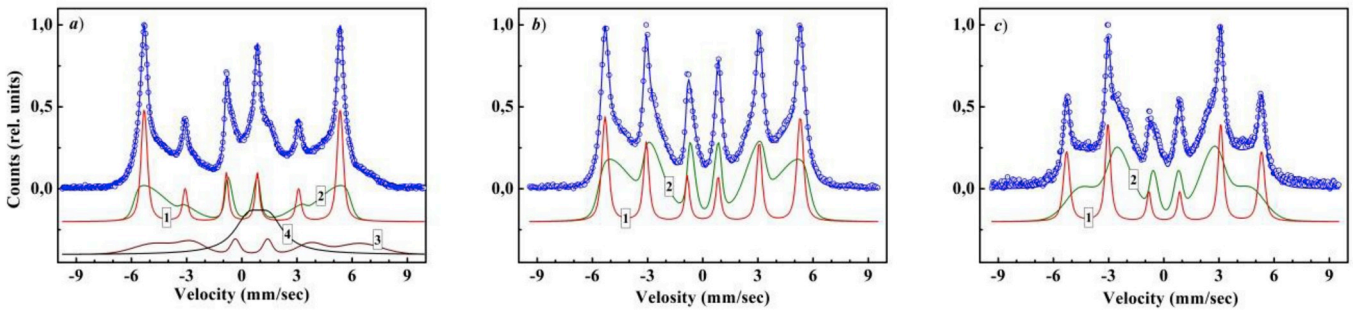

Fig. 5. CEMS spectra of thin Fe films enriched by ^{57}Fe isotope prepared at the deposition rates of: a) 3.2, b) 10 and c) 20 nm/min. Experimental spectra are a superposition of spectral components shown by corresponding thin lines 1.2. . . 4, the hyperfine parameters of which are listed in Table 1.

Table 1
Hyperfine parameters and percentage content of Mössbauer spectral components for ^{57}Fe films prepared at different deposition rates.

	I_S, mm/s	Q_S, mm/s	B_s, T	S, %	A_2, *arb.un.*	θ (deg.)
3.2 nm/min						
Sextet 1 (red, nanocrystalline α- phase of Fe)	0.01	0.01	33.0	26.(0)	0.75	34.2
Sextet 2 (green, disordered α- phase of Fe)	0.04	−0.02	29.4	33.(1)	0.45	26.73
Sextet 3 (dark red, disordered finely dispersed phase with a magnetite-like local environment)	0.69	0.33	34.4	18.(3)	1.84	52.5
Doublet (superparamagnetic magnetite-like clusters and $Fe_{1-x}O$)	0.92	1.14(4)	–	22.(6)	–	–
10 nm/min						
Sextet 1 (red, nanocrystalline α- phase of Fe)	0.00	0.00(2)	32.9	28.(7)	1.94	53.9
Sextet 2 (green, disordered α- phase of Fe)	0.08	−0.02(1)	27.9	69.(0)	1.93	53.8
20 nm/min						
Sextet 1 (red, nanocrystalline α- phase of Fe)	0.02	0.01	32.9	28.(5)	3.6(5)	76.7
Sextet 2(green, disordered α- phase of Fe)	0.09(9)	−0.03(8)	25.7	68.(5)	3.4(6)	74.4

Here I_S is the isomer shift, Q_S is the quadrupole splitting, B_s is the magnetic hyperfine field on the iron nucleus, and S is the relative area of the component in the experimental spectrum. A_2 is the ratio of intensities of the second (fifth) lines of sextet to the third (fourth) lines, and ϕ is the angle between the direction of the magnetic field on nucleus and the wave vector of the resonant gamma photon. The isomer shift and quadrupole splitting errors are about ~0.01 mm/s, the magnetic hyperfine field error is about ~1 T. In brackets, the standard deviations of the measured values are presented as a variation of last digits.

min, only two magnetic sextets are observed (lines 1 and 2 in Fig. 5b and Fig. 5c). In addition to the magnetic components, there is a paramagnetic doublet with a very low intensity (~2% and 3%) in the spectra of these samples (not shown in Fig. 5b and c). Fitting parameters of all Mössbauer spectra are listed in Table 1.

The analysis of the hyperfine parameters listed in Table 1 indicates that the first and second sextets with the isomeric shifts close to zero are attributed to α-phase iron with the bcc lattice and to disordered iron, respectively. The latter is characterized by a wide and asymmetric distribution of hyperfine fields [22]. The mean value of hyperfine magnetic field on the ^{57}Fe nucleus is 29.4 T that is lower than that for α-phase Fe (33.0 T). While increasing the deposition rate, the area *S* under the second sextet, which corresponds to the disordered iron component, increases and exceeds area of the sextet from the crystalline component α-Fe.

The third sextet is present only in the film prepared at a low deposition rate. This sextet has a large isomeric shift ($Is \cong 0.69$) and a wide Gaussian distribution of hyperfine fields with the mean value of 34.4 T. It can be attributed to a disordered finely dispersed phase with a magnetite-like local environment of iron ions (magnetic clusters). The outer 6-th line of this sextet stands out in shape of the broad wing in the range of speed from 6 to 7 mm/s. The isomeric shift of 0.69 mm/s is close to that of the sextet from Fe^{2+} ions in the octahedral positions of magnetite, Fe_3O_4 [23,24]. The strong broadening of sextet lines and the decrease in the mean hyperfine magnetic field for these magnetic clusters is probably due to the wide size distribution of these clusters as well as coherence lengths of magnetic ordering and the presence of carbon impurity in the local environment which lead to the decrease in the magnetic field on the nucleus. The carbon concentration in this sample is about 6–8 at.% according to the elemental analysis. For small clusters with sizes less than 5 nm, the blocking temperature becomes lower than room temperature and superparamagnetism leads to the degeneracy of the sextet structure into a broad absorption line in the central part of the spectrum [24].

The superparamagnetic component is shown by line no. 4 in Fig. 5a. The low-temperature measurements (not shown) of the film synthesized at the low deposition rate of 3.2 nm/min showed that the relative fraction of the superparamagnetic doublet is reduced and the area of the sextet (no. 3) corresponding to magnetite-like clusters increases during lowering of temperature. In addition, we assume that iron oxide $Fe_{1-x}O$ (wüstite) particles also contribute to this superparamagnetic doublet. First, the isomeric shift of 0.92 mm/s is close to that of wüstite (0.86 mm/s). There is a significant quadrupole splitting $Q_S = 1.14$ mm/s (0.78 mm/s for wustite). Secondly, this assumption is consistent with the X-ray structural analysis as is shown below, and also with the results of electron microdiffraction studies of similar samples [18].

It is well known [25] that the ratio (A_2) of intensities of the second (or fifth) sextet line to the third (or fourth) line of the magnetic components of Mössbauer spectra depends on the angle between the direction of the sample magnetization vector and the direction of gamma photon incidence on the sample:

$$A_2 = \frac{4 \cdot sin^2\phi}{1 + cos^2\phi}$$

where ϕ is the angle between the direction of the magnetic field on the nucleus (collinear with the direction of the magnetization vector) and the wave vector of resonant gamma photon (collinear with the direction of the normal to the film plane). $A_2 = 4$ in the case of a thin magnetic film when the magnetization lies in the plane of the film ($\phi = 90^\circ$). The deviation of this ratio from 4 indicates the presence of the perpendicular component of the magnetization vector due to the PMA effect in the magnetic film. The angles ϕ calculated by using fitting parameters of the magnetic components and the abovementioned expression are listed in Table 1. It can be seen that the angles ϕ vary in the range from 26 up to 77° for different magnetic phases (sextets) of iron films prepared at different deposition rates. Note that the minimum values of the angle ϕ (or the maximum angle between the film plane and the magnetization vector) are observed for magnetic sextets in the first sample prepared at the low deposition rate of 3.2 nm/min. Thus, our Mössbauer studies support the presence of the PMA in the films prepared at low and medium deposition rates. Note that these angles can be considered only as qualitative estimates since ϕ = 77° for the iron film prepared at the highest deposition rate of 20 nm/min ($A_2 = 3.6$). The magnetization measurements (Figs. 2c and 3) show that this iron film has no PMA so the sample magnetization should be in the film plane and the angle ϕ be closer to 90°.

2.4. X-ray diffraction analysis

X-ray diffraction patterns of all samples measured in the conventional 2θ geometry reveal only one weak and strongly broadened reflex, which can be attributed to the (110) plane of iron. All studied iron films exhibit the texture since the reflections from other crystalline iron planes are not detected in the conventional Bragg geometry. The reflex peak position is $2\theta = 43.3$, 43.75 or 43.75° for iron films prepared at low (3.2), medium (10) and highest (20 nm/min) deposition rates, respectively (see Fig. 6). These positions of the reflex peak are shifted to the low-angular region of XRD patterns with respect to $2\theta = 44.7$ expected for (110) reflex for pure α-phase Fe [26]. Moreover, XRD patterns of the samples prepared at the deposition rates of 3.2 and 10 nm/min have an asymmetrical shape (Fig. 6a and b). Note that previously the same asymmetric peak was recorded for composite CoO_x films with PMA in Ref. [9]. There is a shoulder in reflex shape from the side of smaller diffraction angles. The intensity of this shoulder decreases while

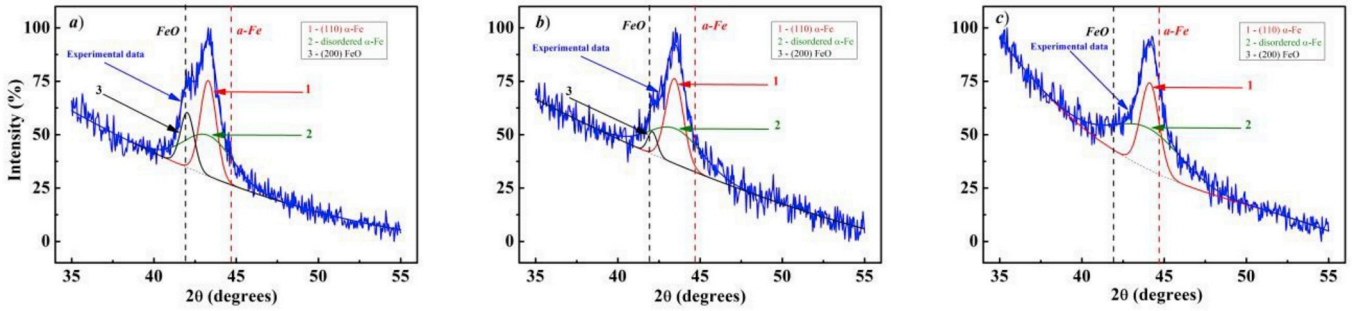

Fig. 6. XRD patterns of iron films prepared on quartz substrates at the deposition rates of: a) 3.2, b) 10 and c) 20 nm/min. Here the dashed lines show the reference peak positions for the (110) reflex of α-phase Fe and the (200) reflex of iron oxide, FeO [26]. The decomposition components of XRD patterns are presented by thin line 1, 2 and 3 are related to (110) α-Fe, disordered Fe and (200) FeO, respectively.

increasing deposition rate and the shoulder disappears in the XRD pattern of the sample deposited at the highest rate of 20 nm/min. Thus, there is a correlation between the intensity of shoulder and the PMA values observed in iron films.

Taking into account the results of Mössbauer studies, the XRD patterns were decomposed into three Fe-based phase components: FeO, α-Fe and "disordered" iron by using the Gauss function for individual components. Note that wüstite (FeO) was used for fitting so the FeO phase has an intense (200) reflex with an angle of $2\theta = 41.99^{\circ}$ [26] close to the position of the observed experimentally peaks. Thin lines 1, 2 and 3 in Fig. 6 show these decomposition components in XRD patterns. It follows from the fitting that the experimental peaks in the XRD patterns is due to the (110) reflex of α-phase Fe as well as the broadened (110) reflex from the disordered iron component. The line 3 correspond to the intense (200) reflex of iron oxide FeO.

The parameters of the XRD pattern decomposition and the calculated lattice constants of structural phase components are listed in Table 2. It is clearly seen that a significant positive deformation of the iron crystal lattice is observed in all studied films (see the last column in Table 2), which depends strongly on the deposition rate. Moreover, the lattice deformation is more than an order of magnitude greater than the limit of the elastic deformation of bulk iron (about 0.1–0.2%) [27]. This fact can be explained by the absence of dislocations in iron nanocrystallites. The analysis of X-ray diffraction data measured in grazing geometry at the incidence angle of $\alpha = 1$, 2, and 3° shows that the position of the most intense (110) reflex does not depend on the incidence angle α for the sample prepared at the low deposition rate of 3.2 nm/min. Therefore, we can conclude that there are no unidirectional macrostresses in iron films, and individual iron nanocrystallites are uniformly deformed (stretched) in all crystallographic directions as it was observed earlier in Ref. [28].

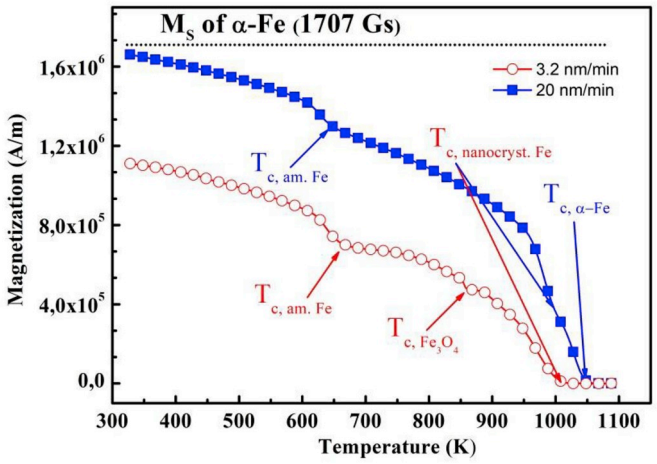

Fig. 7. Temperature dependences of the in-plane magnetization of the iron film prepared at the deposition rates of: 3.2 nm/min (open circles) and 20 nm/min (filled squares).

2.5. Differential thermomagnetic analysis

The additional characterization of the magnetic phase composition of the iron films was carried out by the DTMA method. Fig. 7 shows thermomagnetic curves for iron films prepared on silicon substrates at the deposition rates of 3.2 and 20 nm/min. The iron film with the strong PMA (the deposition rate of 3.2 nm/min) is characterized by three magnetic phases with different Curie temperatures (T_C). These magnetic phases can be attributed to the disordered phase of iron with the low $T_{C,\ am\text{-}Fe} \cong 660$ K [29,30], magnetite phase ($T_{C,\ Fe3O4} \cong 860$ K [30]) and nanocrystalline α-phase Fe with $T_{C,\ nanocryst.} \cong 1010$ K. Note that Curie temperature for nanocrystalline α-phase Fe is lower than the

Table 2
Decomposition parameters of the XRD patterns of iron films prepared at three different deposition rates.

№	2θ (degrees)	FWHM Δ2θ (degrees)	Peak area (%)	Lattice constant a (nm)	$\sigma = \Delta a/a_o^*$ (%)
3.2 nm/min					
1	43.3 (α-Fe, (110))	1.227	40.6	0.29553	3.1
2	43.3 (disordered α-Fe)	3.774	41.3	0.29553	3.1
3	42.015 (FeO, (200))	0.977	18.1	0.43006	−0.1
10 nm/min					
1	43.75 (α-Fe)	1.305	37.62	0.29259	2.1
2	43.75 (disordered α-Fe)	2.818	56.83	0.29259	2.1
3	42.27 (FeO)	1.149	7.59	0.42756	−0.7
20 nm/min					
1	44.137 (α-Fe, (110))	1.36	46.3	0.29018	1.2
2	44.087 (disordered α-Fe)	3.08	57.3	0.29048	1.3

a_0^* - standard value of lattice constants for α-Fe (0.2866 nm) and FeO (0.4303 nm).

T_C value for bulk Fe ($T_{C,\ \alpha-Fe}$ = 1043 K [30]). This result can be explained by the decrease in the exchange interaction due to the increase in the interatomic distance by 3%, as it follows from the X-ray diffraction analysis. In addition, the sample magnetization at room temperature is about 30% less than that for pure α-Fe. This fact supports our Mössbauer and XRD results on the presence of the FeO phase which is nonmagnetic at room temperature. FeO is an antiferromagnetic material with the Néel temperature of T_N = 198 K [30]. Two magnetic phases, disordered and nanocrystalline iron, with T_C ~750 K and 1010 K, respectively, were detected in the iron film deposited at the highest rate of 20 nm/min. This sample has no magnetite phase, but there is a phase with the Curie temperature of α-phase bulk Fe. This means that a significant fraction of iron in this film is in the relaxed (unstressed) state. The saturation magnetization for this sample is close to the magnetization of α-Fe at room temperature.

Our studies of the microstructure and elemental-phase composition of the iron films showed that the source of the strong PMA is the formation of iron oxide phases during the deposition that leads to microstresses. The maximum microstresses were observed in the films prepared at the low deposition rate (3.2 nm/min). With increasing deposition rate (up to 20 nm/min.), the microstresses and the PMA decrease.

We assume that the homogeneous microdeformation of iron nanocrystallites leads to the appearance of additional magnetic moments in all directions due to the magneto-elastic effect. Averaging out of these moments in the film plane yields zero due to the random orientation of iron crystallites in the film plane. However, due to the texture structure of the films, the "induced" magnetic moments of nanocrystallites in the perpendicular direction are summed. As a result, the PMA appears.

We attribute the formation of iron oxide phases and microstresses in the iron films prepared at the low deposition rate to the features of the IBAD technique.

Thus, it follows that the deposition rate significantly affects the structural-phase composition of the films. This is explained by the fact that several fluxes of atoms and ions fall on the substrate surface during the deposition of films, namely: the flux of accelerated xenon ions J_1, which falls on surface of growing film at a grazing angle α_1, the flux of sputtered iron atoms J_2 and the flux of atoms of residual atmosphere (carbon, oxygen and xenon) of vacuum chamber J_3 (see Fig. 1).

At the low deposition rate (3.2 nm/min), when the fluxes J_2 and J_3 are comparable, carbon and oxygen atoms are captured and magnetite-like clusters containing carbon and iron oxide impurities are formed in the addition to α-Fe. Relatively “pure” iron films are formed at high deposition rates (10 and 20 nm/min), when $J_2 \gg J_3$.

First, it is well known that accelerated ions (flux J_1) are reflected from the target surface at grazing angles of incidence. Typically, ions experience multiple small-angle scattering on the surface atoms and transfer a small part of the kinetic energy to these atoms. One ion which falls at the grazing angle can create several low-energy recoil atoms with the momentum directed perpendicular to the surface. Through this process, recoil atoms are implanted into the thin surface region of film and, as a result, stresses are created. The stresses depend on the angle of the ion beam divergence and the deposition rate of films – higher velocity and smaller angle lead to less stress. The energy E of xenon ions was 1 keV, 1.3 keV and 1.5 keV for deposition rates of 3.2 nm/min, 10 nm/min and 20 nm/min, respectively. In this case, the angle of ion beam divergence α_1 was reduced by 5° and was approximately α_1 = 1.5 for E = 1.5 keV. The lattice deformation decreased from 3.1% to 1.2% for the films prepared at the deposition rates of 3.2 nm/min and 20 nm/min, respectively (Table 2) but still remains quite large compared with the limit of the elastic deformation for metals. Therefore, we believe that there is an additional process of the generation of the lattice deformation, which is associated with the implantation of the most high-energy part of sputtered iron atoms (J_2) into the near-surface region of the growing iron film during deposition. This process is valid for all deposition rates used in our work. Both processes have a non-equilibrium character and lead to the uniform increase in the interatomic distance and also to the increase in the interatomic distance due to the incorporation of iron atoms in the interstitial positions. Furthermore, at the low deposition rates atoms of residual atmosphere of the vacuum chamber are trapped, as it was mentioned above.

3. Conclusions

Textured nanocrystalline thin iron films were formed by ion-beam-assisted deposition at the deposition rates of: 3.2, 10 and 20 nm/min under high vacuum conditions. Magnetic properties, structural and phase composition were studied using a wide range of methods. The films have a nanocrystalline structure with a significant fraction of the disordered phase, and the phase composition of films depends significantly on their deposition rate. In addition, films are characterized by a significant positive deformation of the crystal lattice (up to 3%) of nanocrystalline α-Fe, which is associated with the features of the ion-beam-assisted deposition. The increase in the interplanar spacing leads to the reduction of the ferromagnetic Curie temperature of α-Fe. A significant fraction of the nonmagnetic FeO phase is present in iron thin films at the low deposition rate. The FeO phase occurs due to the reaction of iron atoms with the residual atmosphere of the vacuum chamber. The perpendicular magnetic anisotropy is observed for iron films deposited at low and medium rates, which is independent of the film thickness. The iron film free of the substrate also exhibits the PMA. We assume that the origin of the appearance of the PMA in the iron films are microstresses and the magnetoelastic effect. Microstresses can occur due to the formation of secondary nonmagnetic phases, such as FeO in the film volume.

Acknowledgments

Lyadov N.M. is grateful to the Russian Foundation for Basic Research (project no. 18-32-00203) for the financial support of these studies.

References

[1] S.A. Wolf, D.D. Awschalom, R.A. Buhrman, J.M. Daughton, S. von Molnάr, M.L. Roukes, A.Y. Chtchelkanova, D.M. Treger, Spintronics: a spin-based electronics vision for the future, Science 294 (2001) 1488–1495 https://doi.org/10.1126/science.1065389.

[2] Igor Zutic, S. Jaroslav Fabian, Das sarma, Spintronics: fundamental and applications, Rev. Mod. Phys. 76 (2) (2004) 323–410 https://doi.org/10.1103/RevModPhys.76.323.

[3] A.A. Bukharaev, A.K. Zvezdin, A.P. Pyatakov, Yu.K. Fetisov, Straintronics: a new trend in micro- and nanoelectronics and material science, Phys.-Usp. 61 (12) (2018) 1175–1212 https://doi.org/10.3367/UFNe.2018.01.038279.

[4] D.P. Pappas, K.P. Kämper, H. Hopster, Reversible transition between perpendicular and in-plane magnetization in ultrathin films, Phys. Rev. Lett. 64 (26) (1990) 3179–3182 https://doi.org/10.1103/PhysRevLett.64.3179.

[5] B. Heinrich, Z. Celinski, J.F. Cochran, A.S. Arrott, K. Myrtle, Magnetic anisotropies in single and multilayered structures, J. Appl. Phys. 70 (1991) 5769–5774 https://doi.org/10.1063/1.350156.

[6] J.I. Hong, S. Sankar, A.E. Berkowitz, W.F. Egelhoff Jr., On the perpendicular anisotropy of Co/Pd multilayers, J. Magn. Magn. Mater. 285 (2005) 359–366 https://doi.org/10.1016/j.jmmm.2004.07.054.

[7] M. Coisson, F. Celegato, E. Olivetti, P. Tiberto, F. Vinai, M. Baricco, Stripe domains and spin reorientation transition in $Fe_{78}B_{13}Si_9$ thin films produced by rf sputtering, J. Appl. Phys. 104 (2008) 033902-1-033902-7 https://doi.org/10.1063/1.2960454.

[8] L. Xi, J.M. Lu, J.J. Zhou, Q.J. Sun, D.S. Xue, F.S. Li, Thickness dependence of magnetic anisotropic properties of FeCoNd films, J. Magn. Magn. Mater. 322 (2010) 2272–2275 http://doi.org/10.1016/j.jmmm.2010.02.024.

[9] T. Ichikawa, N. Hiratsuka, S. Kobayashi, M. Sugimoto, Perpendicular magnetic anisotropy of CoO_x films prepared by targets facing type of sputtering, IEEE Transl. J. Magn. Jpn. 6 (11) (1991) 994–1000 https://doi.org/10.1109/TJMJ.1991.4565293.

[10] B. Schulz, K. Baberschke, Crossover from in-plane to perpendicular magnetization in ultrathin Ni/Cu(001) films, Phys. Rev. B 50 (18) (1994) 13467–13471 https://doi.org/10.1103/PhysRevB.50.13467.

[11] A.S. Kamzin, Fulin Wei, V.R. Ganeev, A.A. Valiullin, L.D. Zaripova, L.R. Tagirov, Influence of the film thickness and additional elements (Al, O, and N) on the properties of FeCo film structures, Phys. Solid State 56 (5) (2014) 914–920 https://doi.org/10.1134/S1063783414050114.

[12] I.A. Faizrakhmanov, V.V. Bazarov, V.A. Zhikharev, I.B. Khaibullin, Optical and electrical properties of C^+-implanted amorphous diamond-like carbon films, Nucl. Instr. Meth. Phys. Res. B 127/128 (1997) 719–722 https://doi.org/10.1016/S0168-583X(96)01164-0.
[13] A.L. Stepanov, B.N. Chichkov, V.F. Valeev, V.I. Nuzhdin, I.A. Faizrakhmanov, Modification of ion-synthesized silver nanoparticles in glass by high-power excimer laser pulses, Tech. Phys. Lett. 34 (12) (2008) 184–186 https://doi.org/10.1134/S1063785008030024.
[14] N.I. Khalitov, V.F. Valeev, R.I. Khaibullin, I.A. Faizrakhmanov, P.A. Gorbatova, V.V. Parfenov, K.E. Prikhodko, V.V. Roddatis, M.Yu. Presniakov, M. Maksutoglu, F.A. Mikailzade, Structural, magnetic and magnetoelectric studies of $BaTiO_3$:Co nanocomposite films formed by ion-beam methods, Nucl. Instr. Meth. Phys. Res. B 331 (2014) 163–167 https://doi.org/10.1016/j.nimb.2014.01.033.
[15] H.A. Novikov, R.I. Batalov, R.M. Bayazitov, I.A. Faizrakhmanov, G.D. Ivlev, S.L. Prokop'ev, Optical diagnostics of the laser-induced transformations in thin germanium films on silicon, sapphire, and fused silica, Tech. Phys. 60 (3) (2015) 406–412 https://doi.org/10.1134/S1063784215030214.
[16] H.A. Novikov, R.I. Batalov, R.M. Bayazitov, I.A. Faizrakhmanov, N.M. Lyadov, V.A. Shustov, K.N. Galkin, N.G. Galkin, I.M. Chernev, G.D. Ivlev, S.L. Prokop'ev, P.I. Gaiduk, Pulsed modification of germanium films on silicon, sapphire, and quartz substrates: structure and optical properties, Semiconductors 49 (6) (2015) 746–752 https://doi.org/10.1134/S1063782615060160.
[17] N.M. Lyadov, A.I. Gumarov, V.F. Valeev, V.I. Nuzhdin, V.V. Bazarov, I.A. Faizrakhmanov, Optical properties of ZnO and Al_2O_3 implanted with silver ions, Tech. Phys. 59 (5) (2014) 62–65 https://doi.org/10.1134/S106378421405020X.
[18] N.M. Lyadov, V.V. Bazarov, F.G. Vagizov, I.R. Vakhitov, E.N. Dulov, R.N. Kashapov, A.I. Noskov, R.I. Khaibullin, V.A. Shustov, I.A. Faizrakhmanov, Structural and magnetic studies of thin Fe^{57} films formed by ion beam assisted deposition, Appl. Surf. Sci. 378 (2016) 114–119 https://doi.org/10.1016/j.apsusc.2016.03.193.
[19] D.K. Nurgaliev and P.G. Yasonov, RF Patent No. 81805, Byull. Izobret., 9 (2009).
[20] B. Bourov, P. Iasonov, D. Nourgaliev, Sh. Ibragimov, Thermomagnetic analysis using a high heating rate, Ann. Geophys. 14 (1) (1996) 133.
[21] L.M. Alvarez-Prado, J.M. Alameda, Micromagnetism of nanowires with low out-of plane-anisotropy, Physica B 343 (2004) 241–246 https://doi.org/10.1016/j.physb.2003.08.101.
[22] G.J. Long, D. Hautot, Q.A. Pankhurst, D. Vandormael, F. Grandjean, J.P. Gaspard, V. Briois, T. Hyeon, K.S. Suslick, Mössbauer-effect and x-ray-absorption spectral study of sonochemically prepared amorphous iron, Phys. Rev. B 57 (17) (1998) 10716–10722 https://doi.org/10.1103/PhysRevB.57.10716.
[23] J.M.D. Coey, A.H. Morrish, G.A. Sawatsky, A Mössbauer study of conduction in magnetite, J. Phys. Colloq. 32 (1971) C1-271-C1-273 https://doi.org/10.1051/jphyscol:1971190.
[24] C.E. Johnson, J.A. Johnson, H.Y. Hah, M. Cole, S. Gray, V. Kolesnichenko, P. Kucheryavy, G. Goloverda, Mössbauer studies of stoichiometry of Fe_3O_4: characterization of nanoparticles for biomedical applications, Hyperfine Interact. 237 (2016) 27-1-27-10 https://doi.org/10.1007/s10751-016-1277-6.
[25] G.K. Wertheim, Mössbauer Effect, Elsevier Inc., Academic Press, 1964, https://doi.org/10.1016/C2013-0-12103-4.
[26] L.I. Mirkin, Handbook of X-Ray Analysis of Polycrystalline Materials, Consultants Bureau, New York, 1961.
[27] A.M. Sarosiek, W.S. Owen, The work hardening of dual-phase steels at small plastic strains, Mater. Sci. Eng. 66 (1984) 13–34 https://doi.org/10.1016/0025-5416(84)90138-1.
[28] M.W. Grinstaff, M.B. Salamon, K.S. Suslick, Magnetic properties of amorphous iron, Phys. Rev. B. 48 (1993) 269–273 https://doi.org/10.1103/PhysRevB.48.269.
[29] M. Vázquez, R. ElKammouni, G.V. Kurlyandskaya, V. Rodionova, L. Kraus, Biomagnetic microwires, magnetic properties, and high-frequency behavior, in: A. Zhukov (Ed.), Novel Functional Magnetic Materials. Springer Series in Materials Science, vol 231, Springer, Cham, 2006, pp. 279–310 https://doi.org/10.1007/978-3-319-26106-5_7.
[30] Ch. Kittel, Introduction to Solid State Physics, Wiley, 1996.